Research Article

Nano Research
2024, 17(7): 6654–6660

ISSN 1998-0124 CN 11-5974/O4
https://doi.org/10.1007/s12274-024-6582-9

Fine-tuning growth in gold nanostructures from achiral 2D to chiral 3D geometries

Lili Tan, Zhi Chen, Chengyu Xiao, Zhiyong Geng, Yinran Jin, Chaoyang Wei, Fei Teng, Wenlong Fu, and Peng-peng Wang (✉)

State Key Laboratory for Mechanical Behavior of Materials, Shaanxi International Research Center for Soft Matter, School of Materials Science and Engineering, Xi'an Jiaotong University, Xi'an 710049, China

Received: 18 December 2023 / **Revised:** 5 February 2024 / **Accepted:** 21 February 2024

ABSTRACT

Enriching the library of chiral plasmonic structures is of significant importance in advancing their applicability across diverse domains such as biosensing, nanophotonics, and catalysis. Here, employing triangle nanoplates as growth seeds, we synthesized a novel class of chiral-shaped plasmonic nanostructures through a wet chemical strategy with dipeptide as chiral inducers, including chiral tri-blade boomerangs, concave rhombic dodecahedrons, and nanoflowers. The structural diversity in chiral plasmonic nanostructures was elucidated through their continuous morphological evolution from two-dimensional to three-dimensional architectures. The fine-tuning of chiroptical properties was achieved by precisely manipulating crucial synthetic parameters such as the amount of chiral molecules, seeds, and gold precursor that significantly influenced chiral structure formation. The findings provide a promising avenue for enriching chiral materials with highly sophisticated structures, facilitating a fundamental understanding of the relationship between structural nuances and chiroptical properties.

KEYWORDS

plasmonic nanostructures, geometric chirality, circular dichroism, fine-tuning

1 Introduction

Chirality, an asymmetrically geometric property, has been exploited as a focal point across diverse scientific domains, spanning from organics to inorganics realms [1–5]. This exploration has been propelled by interdisciplinary studies driven by remarkable advancements in nanoscience and technology [6–10]. Of particular intriguing are nanostructured geometrically chiral plasmonic materials, which display unprecedented and tunable chiroptical properties due to their robust asymmetric light–matter interaction that stems from the highly sensitive local surface plasmon resonance to size, shape, and dielectric environment [11–14]. These materials hold tremendous potentials for various applications, such as polarization-dependent photochemical reactions, chiral sensing, photonics, and biotherapy [15–18]. Various top–down and bottom–up strategies have been deliberately developed for the preparation of chiral plasmonic nanomaterials [19–22]. Among these strategies, the seed-mediated wet-chemical method has received increasing interest as it offers a facile and scalable means of engineering morphological control within chiral plasmonic colloidal nanostructures, thereby enabling chiroptical tunability [23–25]. However, despite considerable efforts, the diversity in structural and chiroptical properties of chiral plasmonic nanostructures remains relatively limited, and establishing precise relationships between them remains a challenge.

In this study, we report a novel class of chiral plasmonic nanostructures with rich chiral morphologies and adjustable chiroptical responses. Employing the seed-mediated growth method, we have achieved a diversity of geometrically chiral plasmonic nanostructures starting from initially achiral two-dimensional (2D) gold triangle nanoplates (TNPs) acting as seeds. These achiral 2D seeds underwent controlled growth, evolving into a series of chiral nanostructures including tri-blade boomerangs, concave rhombic dodecahedrons (RDs), and nanoflowers. Furthermore, fine-tuning synthesis parameters on the basis of the resulting plasmonic nanostructures not only enrich structural diversity but also allow for the modulation of chiroptical activity. This provides a promising platform to explore and understand the relationship between chiral structure and chiroptical properties.

2 Results and discussion

Our approach involves a seed-mediated method to construct chiral colloidal Au nanoparticles (NPs), as illustrated in Fig. S1 in the Electronic Supplementary Material (ESM). This process mainly involves the chiral growth of 2D Au TNPs acting as seeds in presence of chiral enantiomers. To synthesize the chiral Au nanostructures with diverse geometries, anisotropic Au TNPs were pre-synthesized as growth seeds [10, 26]. As observed in the transmission electron microscopy images (Fig. S2 in the ESM), these as-obtained NPs appear as 2D TNPs with edge lengths of ~ 70 nm, and their purity level exceeds 90%. The analysis of high-resolution transmission electron microscopy image and the corresponding fast Fourier transform pattern of the TNP reveals

Address correspondence to ppwang@xjtu.edu.cn

清華大學出版社 Tsinghua University Press Springer

the existence of twin planes or stacking faults (Fig. S3 in the ESM) [27–29]. Subsequently, these 2D TNPs serve as seeds for overgrowth into chiral Au NPs, employing L-glutathione-phenylalanine (GP) as a chiral ligand, ascorbic acid (AA) as a reducing agent, cetyltrimethylammonium chloride (CTAC) as a surfactant, and gold chloride trihydrate ($HAuCl_4$) as the metal ion precursor, respectively. The resulting morphologies and chiroptical properties of chiral NPs strongly depend on these reaction parameters. Notably, the amount of gold precursor plays a critical role in the structural evolution of chiral NPs by influencing the quantity of gold atoms deposited on the triangular Au seeds and, consequently, affecting the optical properties [30, 31].

Interestingly, adjusting the addition amount of gold precursor while maintaining other synthetic conditions unchanged leads to the formation of chiral Au NPs with diverse morphologies. Figure 1 illustrates a series of chiral NPs, including chiral tri-blade boomerangs, wrinkled concave RDs, and multibranched nanoflowers, obtained by varying the amount of gold precursor. Initially, chiral tri-blade boomerangs emerge from TNPs when the amount of gold precursors is relatively low. Gradually increasing the gold precursor amount results in successive overgrowth from 2D seeds, leading to the construction of three-dimensional (3D) chiral nanostructures including concave RDs and ultimately nanoflowers with protruding edges. For instance, with a lower amount of gold precursor in the aqueous solution (0.017 mM), tri-blade boomerangs are observed (Fig. 2(a)). As the concentration of gold precursor increases further (0.025 mM), the propellers widen, resulting in the expansion of their three paddles (Fig. 2(b)). A moderate amount of gold precursor leads to the production of concave RD NPs with distinct valleys (Figs. 2(d)–2(h)). Within the range of 0.1–1.33 mM of added gold precursor, the resulting chiral NPs predominantly maintain the profile of 3D RDs. However, their sizes expand from approximately 200 to 400 nm, while their inner surfaces become increasingly dented and wrinkled with higher gold precursor concentrations during the reaction process.

Once gold precursor concentration exceeds 1.67 mM, a notable transformation in the surface of the prepared chiral Au NPs occurs, resulting in highly uneven 3D nanoflowers with protruding spikes (Figs. 2(i)–2(l)). This excessive amount of gold precursor not only triggers the transformation of the morphology of chiral nanoparticles from wrinkled concave RDs to larger-sized nanoflower structures (600–700 nm), but also greatly increases the surface roughness of the NPs. The reduction rate in the reaction system is directly proportional to the gold precursor amount with constant and excessive reducing agent AA, which affects the evolution of structure [32, 33]. Consequently, increasing the gold precursor quantity in the reaction solution can lead to faster

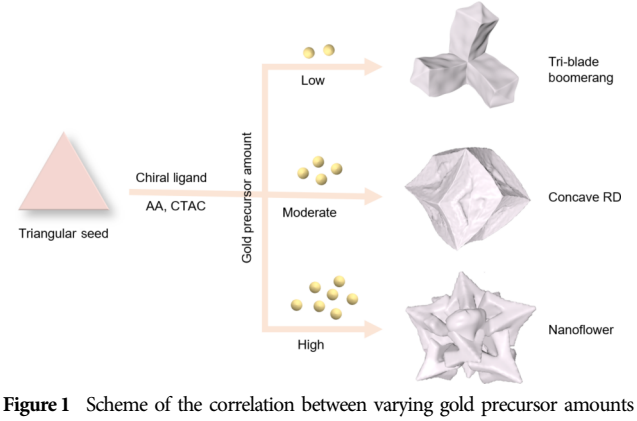

Figure 1 Scheme of the correlation between varying gold precursor amounts and the resulting morphological variation in chiral Au NPs: tri-blade boomerangs, concave RDs, and nanoflowers.

reduction rate and higher supersaturation, facilitating the formation of NPs with higher surface energy [25, 33–35].

The control of the gold precursor amount imparts distinct morphologies of the obtained chiral NPs, crucially impacting their chiral properties. Circular dichroism (CD) spectroscopy was performed to characterize their chiroptical properties of these samples. The CD spectra of chiral Au NPs, prepared with varying concentrations of gold precursors, are shown in Fig. 3. Nanoflowers synthesized with a larger amount of gold precursor exhibit distinct CD signals at 500–800 nm (Fig. 3(a) and Fig. S4 in the ESM). These chiral NPs exhibit a red-shifted optical response in comparison to chiral concave RDs and tri-blade boomerangs synthesized with lower amount of gold precursor. For instance, chiral NPs synthesized with 2.67 mM of gold precursor exhibit a positive CD peak at around 700 nm, whereas those synthesized with 1.67 mM display a positive CD peak at around 650 nm. For RDs with dented surfaces formed with a moderate amount of gold precursor, two positive CD peaks emerge. Based on the RD outline, the gradual emergence of wrinkles and ridges on the concave surface leads to the splitting of transverse resonance, resulting in peak splitting in the CD signals. Distinct CD signals with one negative peak and one positive peak (negative cotton effect) are observed for the NPs obtained with smaller concentration of gold precursor (0.025–0.17 mM), as shown in Fig. 3(b). For example, with 0.025 mM of gold precursor, the synthesized NPs show two CD peaks: a negative peak at ~ 720 nm and a positive CD peak at ~ 600 nm. The positions of these CD responses align with the observed extinction peaks in the extinction spectra (Fig. S5 in the ESM). Upon reaching 0.05 mM, a weak CD signal emerges due to the gradually widening and thickening of the propeller, resulting in the distortion of the chiral morphology. With an increase in the gold precursor amount, the CD signals undergo a blue shift due to the appearance of chiral concave RDs with small size.

Moreover, the processes of nanoparticle formation and growth have been further investigated and analyzed to understand the chiral structural evolution. The gold precursor concentration plays a crucial role in determining the morphology evolution of the nanoparticles by controlling the reduction reaction rate [33]. As shown in Fig. S6 in the ESM, with low concentration of gold precursor, triangle seeds grow into chiral tri-blade boomerangs, indicating preferential growth orientations. Au atom preferentially deposits on the (100) dominated side facets of the triangular seed. This is likely influenced by the existence of twin planes, which results in chiral tri-blade boomerangs NPs with (100) dominated edges [36–38]. Adequate concentration of gold precursor in reaction solution ensures the nuclei on all of sides and facets growing autocatalytically into polyhedral structures [39]. In Fig. S7 in the ESM, we observed characteristic hexagonal outlines of chiral RDs corresponding to the [111] axis and square contours aligned with [100] axis, revealing the concave feature of these NPs. With increased gold precursor concentration, the inner surface of the concave RD frame becomes more rugged. This change can be attributed to an increased rate of the reduction, which preferentially leads to the formation of protruded edges on the NPs. This occurs because the deposition rate of Au atoms exceeds the diffusion rate. As a result, when there is an excess of gold precursors, the deposition rate is faster than the diffusion rate, resulting in island growth and the subsequent formation of chiral nanoflowers.

Chiral GP molecules serve as chiral sources enabling the transfer of chirality to inorganic NPs, influencing their chirality evolution [36, 37]. To understand the impact of chiral molecules, we investigated how their amount affects the final optical properties and morphology of these NPs. We took the chiral

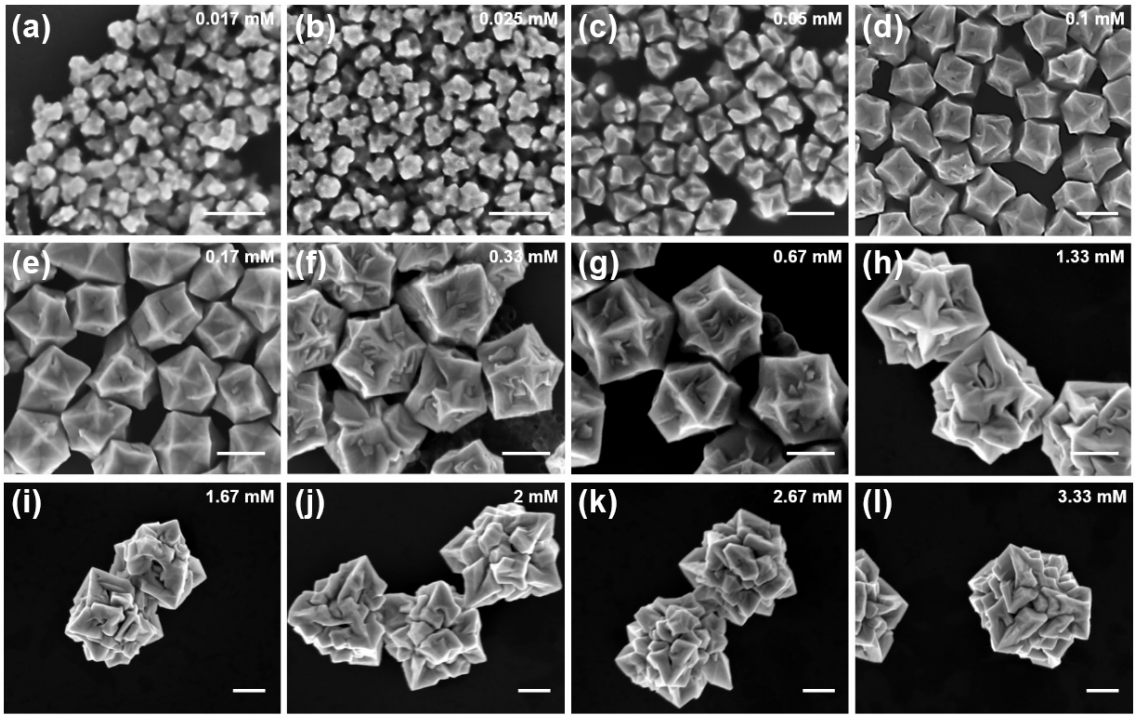

Figure 2 Structural evolution of chiral Au NPs synthesized with varying gold precursor concentrations. (a)–(l) Scanning electron microscopy (SEM) images of chiral Au NPs obtained with different gold precursor concentrations from 0.017 to 3.33 mM. Scale bar, 200 nm.

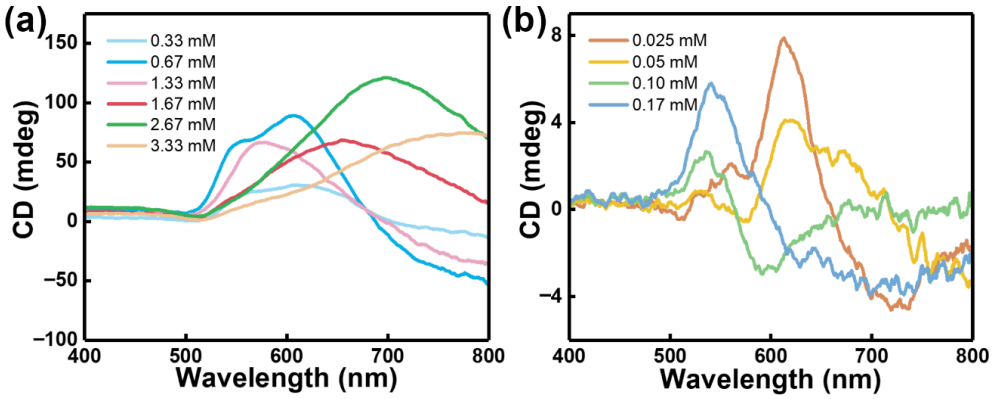

Figure 3 Chiroptical properties of chiral Au NPs with varying gold precursor concentrations. CD spectra of chiral Au NPs synthesized using different gold precursor concentrations: (a) 0.33–3.33 mM and (b) 0.025–0.17 mM.

concave RD NPs synthesized with moderate concentrations of gold precursor (1.33 and 0.5 mM) as examples to examine the effects of GP (Fig. 4). In the reaction systems with 1.33 mM of gold precursor without GP enantiomers, the resulting NPs exhibit an RD shape but lack discernible CD signals (Fig. S8 in the ESM). Introducing chiral GP molecules induces significant changes, transforming the planar smooth RD shape into a concave RD with clearer edges and corners (Figs. 4(a)–4(d)). Even trace amounts of GP (1.3 μM) can trigger the appearance of valleys and steep ridges, indicating active surface growth in the formation of chiral NPs (Fig. 4(a)) [38–40]. Increasing GP amounts amplifies surface distortions and wrinkles, transitioning from ridges to bolded walls, indicating chiral ligands' capability of guiding atomic packing on the growth surface to form ridges or wrinkled surface patterns. When the excessive amounts of GP are used, nanoflowers with rich ridges are developed (Fig. 4(d)). Sizes of these chiral NPs gradually increase from about 450 to 550 nm with increasing the chiral ligand amounts, suggesting an influence on growth dynamics due to the chiral ligands' reducing effect by thiol group oxidation [41, 42]. In reaction systems using 0.5 mM of gold precursor, a similar trend emerges wherein an increase in chiral ligand concentration also leads to enhanced surface roughness, mainly the emergence of wrinkled ridges (Figs. 4(e)–4(h)).

These structural alterations in chiral concave RD NPs correspond to changes in their chiroptical properties (Figs. 4(i) and 4(j) and Fig. S9 in the ESM). Specifically, the wrinkled surface patterns of concave RD NPs result in exceptional optical activity. As shown in Fig. 4(i), all samples obtained with the fixed gold precursor of 1.33 mM and varying GP amounts exhibit strong CD signals, predominantly centered at around 600 nm. An increase in chiral molecule amounts enhances the CD signals in the corresponding NPs. This enhancement trend continues until the chiral molecule amount reaches 20 μM, displaying optimal optical activity attributed to the increased wrinkles on the chiral NP surfaces. Nevertheless, surpassing 20 μM of chiral GP initiates a slight deterioration in the chiroptical properties of the resulting large-sized nanoflower NPs due to randomly distributed protrusions on the surface [43]. Moreover, red shifts in CD peaks are observed with increasing chiral GP amounts. Similarly, under the fixed gold precursor condition of 0.5 mM, adjusting the amount of chiral GP also results in enhancement trend in the chiroptical response of the resulting NPs, which is associated with more pronounced surface patterns (Fig. 4(j) and Fig. S10 in the

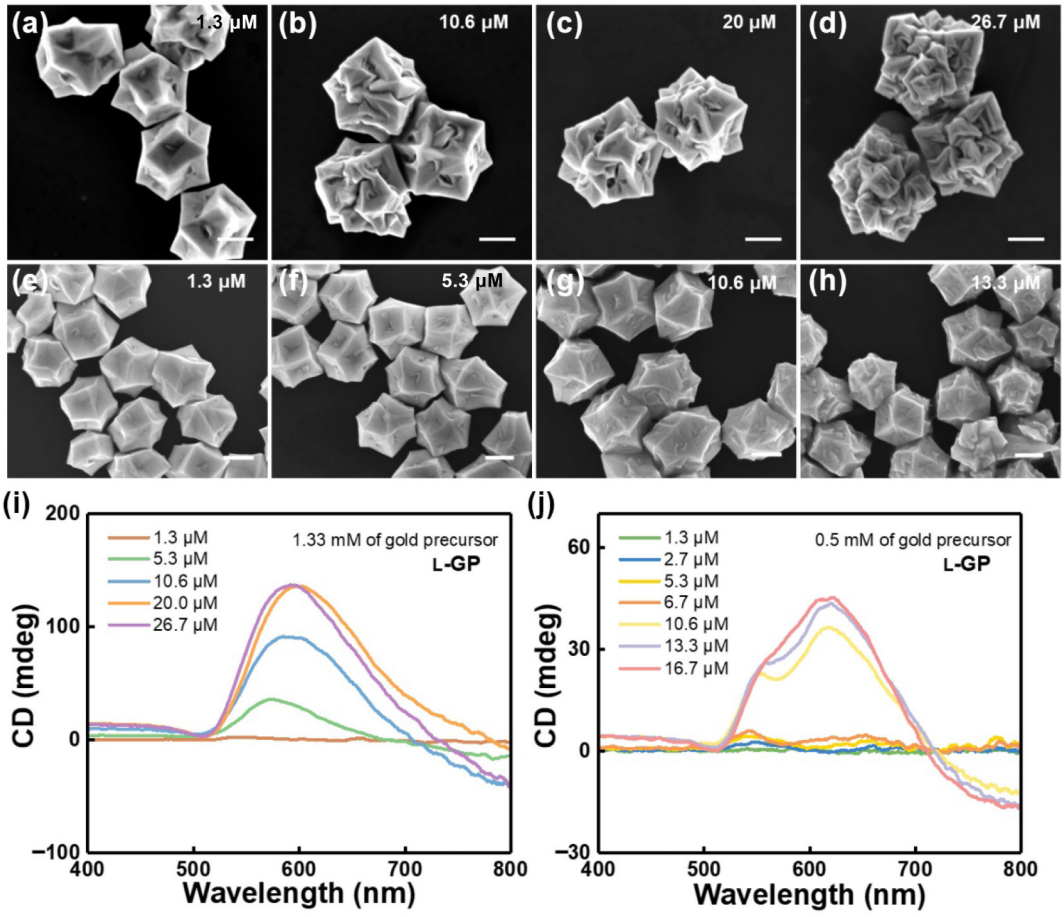

Figure 4 Influence of chiral ligands on the formation of chiral Au NPs. (a)–(d) SEM images of chiral Au NPs synthesized with a fixed gold precursor of 1.33 mM and varying chiral GP concentrations from 1.3 to 26.7 μM. (e)–(h) SEM images of chiral Au NPs synthesized with a fixed gold precursor of 0.5 mM and varying chiral GP concentrations from 1.3 to13.3 μM. (i) CD spectra of chiral Au NPs synthesized with the fixed gold precursor of 1.33 mM and varying chiral GP concentrations from 1.3 to 26.7 μM. (j) CD spectra of chiral Au NPs synthesized with the fixed gold precursor of 0.5 mM and varying chiral GP concentrations from 1.3 to 16.7 μM. Scale bar, 200 nm.

ESM). In the case of chiral tri-blade boomerangs that are synthesized with relatively small concentration of gold precursor (0.025 mM), increasing chiral molecule concentrations (3.3–10 μM) leads to the decrease in NP size from ~ 150 to ~ 128 nm. Excessive chiral ligands (67 μM) capping on TNP seed surface interfere with gold atom deposition and prevent the original seeds from overgrowing into chiral Au NPs (Fig. S11 in the ESM). Suitable amounts of chiral ligands result in chiral tri-blade boomerangs with excellent chiroptical properties, while excess or absence of chiral molecules yields no CD signals (Figs. S12 and S13 in the ESM).

To further explore the growth dynamics of chiral NPs, we studied the time-dependent morphology and optical evolution of chiral concave RD NPs that were synthesized using 0.67 mM of gold precursor and 10.6 μM of L-GP. Observations in Fig. S14 in the ESM reveal concave polyhedron NPs of ~ 200 nm at a reaction time of 5 min. As the reaction time extends, a noticeable transition occurs as these chiral NPs transform into RD shapes. For instance, reaction time of 10 and 15 min yields RD NPs of approximately 270 and 410 nm, respectively. At a reaction time of 60 min, the NP size stabilizes at about 460 nm, yet the wrinkles inside the concave side of the RD NPs significantly deepen. Prolonged reaction time results not only in larger-sized chiral RD NPs but also in enhanced surface patterns. At a 10-min reaction time, a weak CD signal is detected in the obtained NPs (Fig. S15 in the ESM). Upon increasing the reaction time to 15 min, significant CD signals emerge, presenting two peaks at 547 and 638 nm. At a reaction time of 60 min, the resulting chiral NPs exhibit stronger CD signals with peaks at 560 and 657 nm, probably due to the heightened surface wrinkles observed in Fig. S14(d) in the ESM. These results suggest that a gradual enhancement in the optical activities of the NPs is associated with the chiral wrinkles on the surface of NPs.

In addition, we carried out fine-tuning of chiroptical properties and structures of Au NPs by controlling other factors such as the CTAC surfactant, AA reducing agent, and TNP seeds. The surfactant CTAC plays a crucial role in regulating NP nucleation and growth, guiding controlled synthesis of plasmonic NPs [44–46]. Manipulating CTAC concentrations reveals distinct effects on the morphology and optical evolution of chiral Au NPs (Figs. 5(a)–5(d)). Lower CTAC concentration (3.3 mM) results in insufficient stability in the reaction solution, leading to the formation of prominent irregular dendritic structures (Fig. 5(a)). The irregular morphologies weaken the chiroptical response of the resulting chiral NPs, as shown in Fig. 5(e). Conversely, increasing the surfactant concentration (6.7 mM) slows the growth rate of NPs through passivation/facet stabilization [47, 48], and leads to the chiral NPs with gentle and regular branches. This results in well-defined RD structures with protruding edges and enhanced CD signals. Similarly, slight changes in fragmented RD morphologies and optical properties are observed by controlling the AA amount (Fig. S16 in the ESM). This control influences crystal growth kinetics by regulating gold ion reduction rates [36], thus contributing to the observed alterations in NP morphology and optical characteristics.

The impact of TNP seed amounts on the overgrowth from achiral TNPs to varying chiral Au NPs is profound by altering the

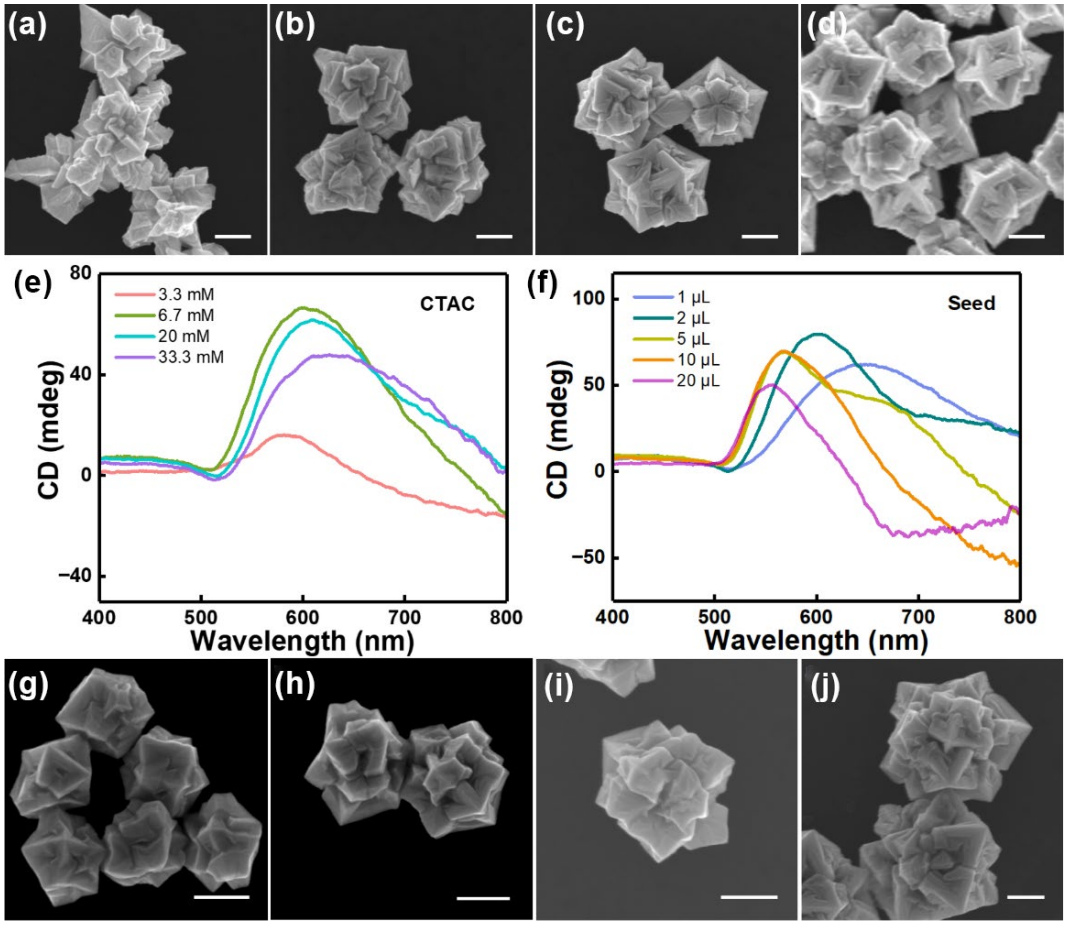

Figure 5 Fine-tuning structures and chiroptical properties of chiral Au NPs by adjusting CTAC and TNP seed amounts. (a)–(d) SEM images and (e) CD spectra of chiral Au NPs with varying CTAC concentrations (3.3, 6.7, 20, and 33.3 mM). (f) CD spectra of chiral Au NPs with varying seed amounts. SEM images of chiral Au NPs with different seeds amounts: (g) 20, (h) 10, (i) 5, and (j) 1 μL. Scale bar, 200 nm.

rate of deposition of reaction [38, 49]. In order to explore the influence, we adjusted the TNP seed addition during chiral concave RD NP synthesis (maintaining a fixed gold precursor of 1.33 mM and GP of 20 μM), as illustrated in Figs. 5(f)–5(j) and Fig. S17 in the ESM. Fewer seeds lead to more pronounced chiral patterns and enhanced CD signals in the resulting chiral NPs. For instance, using 1 μL of TNPs as seeds, the NPs exhibit exaggerated nanoflower structures with angular protrusions, reaching a size of approximately 775 nm (Fig. 5(j)), a consequence of limited seeds during reaction process promoting extensive growth [38]. Moreover, significant red-shifted CD signals, consistent with the extinction spectra (Fig. S17(b) in the ESM), are observed, coinciding with the increased size of resulting chiral NPs (from 280 to 480 nm) as TNP seed amounts decrease from 20 to 5 μL. This decrease in seed amount theoretically corresponds to a simultaneous increase in the amounts of chiral molecule and gold precursor, resulting in expanded NPs [38].

To better illuminate the role of synthetic parameters in controlling chiral structures and their optical responses, we constructed a correlation diagram (Fig. S18 in the ESM) that outlined the structure and chiroptical evolution of NPs with various factors including concentrations of gold precursor, GP, seed, and CTAC. Obviously, the gold precursor serves as the decisive role in determining the morphology of synthesized NPs across a broad concentration range, which results in varying shapes from chiral tri-blade boomerangs (0.025–0.05 mM) and concave RDs (0.1–1.33 mM) to nanoflowers (1.67–3.33 mM). Furthermore, by influencing the dynamics of NP growth, an optimal combination of surfactant concentration and seed amount facilitates the formation of chiral concave RDs. Conversely, lower levels of these parameters favor the generation of chiral nanoflowers with dendritic morphologies, a result of the enhanced growth rate of NPs. It is noteworthy that the presence of a sufficient amount of Au precursor under these conditions inhibits the formation of chiral tri-blade boomerangs. Moreover, the availability of an adequate supply of Au precursor is essential for the role of chiral molecules (GP) in guiding the surface structure evolution of chiral RDs by governing the kinetics of chiral deformation. At lower GP concentrations, the slower kinetics of chiral deformation compared to the kinetics of crystal growth leads to less pronounced chiral features. In contrast, at optimal GP concentrations, the interaction between the ligand and the gold surface is significantly strengthened. This enhanced interaction leads to faster chiral deformation which outpaces the rate of crystal growth. As a result, more pronounced chiral features are developed, characterized by clear wrinkle features with greater curvature and enhanced optical responses. Correspondingly, the chiroptical responses of these NPs vary due to the different plasmonic resonance modes inherent to each morphology.

Another unique characteristic of chiral NPs lies in their enantiomers, exhibiting opposite chiral structures. As shown in Figs. 6(a) and 6(b), chiral concave RDs prepared with enantiomeric chiral ligands display opposite handedness from different angles. This structural chirality can be somewhat ambiguous when viewed from different perspectives. Simplified models are also provided (Fig. 6(c)). The opposite handedness of chiral concave RDs was confirmed by mirror-symmetric optical activities (Fig. 6(d)). Adjusting the amount of added TNP seeds results in an evolution in the chiroptical responses of the resultant

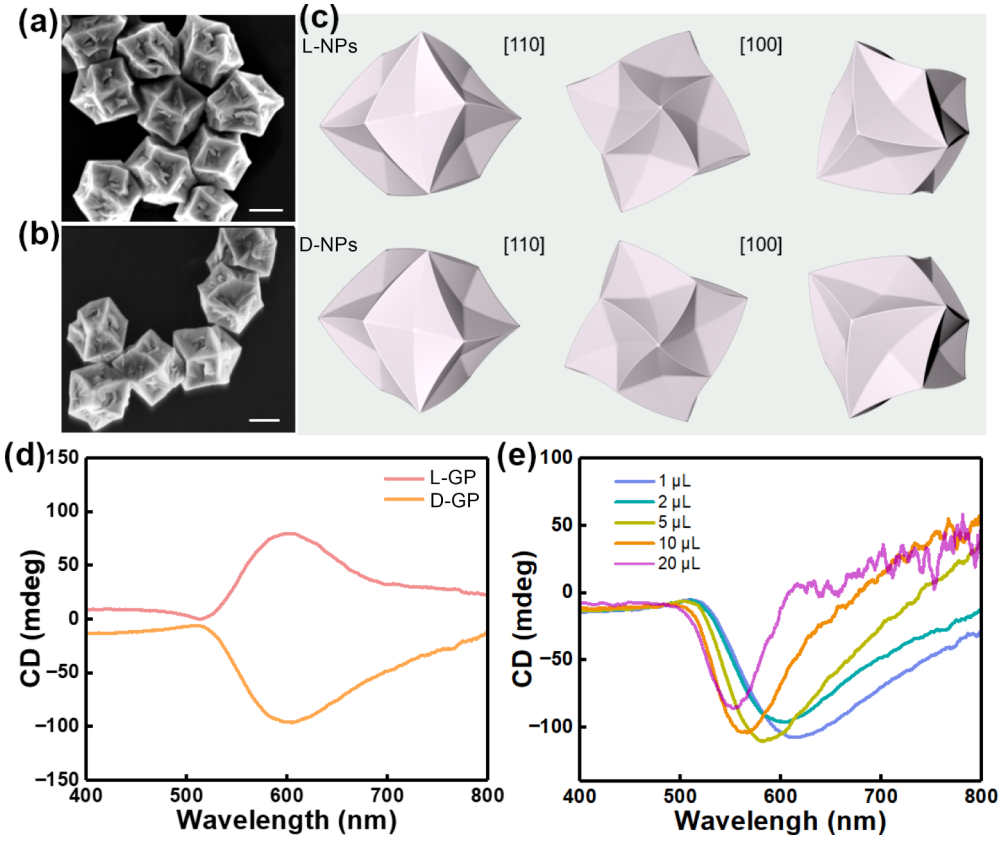

Figure 6 Opposite chirality of Au NPs. (a) and (b) SEM images showing chiral concave RDs synthesized with L-GP and D-GP, respectively. Scale bar, 200 nm. (c) Possible models of chiral concave RD enantiomers projected along [110], [100], and random orientations. It should be noted that these models are idealized and simplified, and as such, may not fully capture the intricate details of the actual NPs. (d) CD spectra of chiral Au NPs synthesized using L-GP and D-GP as chiral molecules. (e) CD spectra of chiral Au NPs synthesized with varying D-GP amounts.

chiral D-NPs (Fig. 6(e) and Fig. S19 in the ESM), aligning with the observations in the discussed L-formed chiral NPs: enhanced and red-shifted chiroptical signals as TNP seed amounts decrease.

3 Conclusions

In conclusion, our work demonstrates the successful synthesis of a diverse range of chiral-shaped Au NPs with complex morphologies and adjustable chiroptical properties through a seed-mediated wet chemical strategy. Starting from the same 2D seeds, our controlled growth processes have enabled the creation of chiral Au NPs in various forms, including chiral tri-blade boomerangs, concave RDs, and nanoflowers. The evolution of these structure intricacies, especially their surface patterns, is intricately influenced by synthesis parameters such as the quantity of chiral ligands and TNP seeds involved in the reaction, resulting in fine-tuning of their chiroptical properties. This capability to tailor optical plasmonic materials with unique architectures significantly enriches the library of chiral inorganic nanostructures and provides a tailored chiral nanoplatform for extensive applications.

Acknowledgements

This work was supported by the National Natural Science Foundation of China (Nos. 22001201 and 22075224) and the Science and Technology Agency of Shaanxi Province (No. 2022KWZ-21). We thank Mr. Jiawei Wang, Ms. Jiao Li, and Ms. Fuchun Tan at Instrumental Analysis Center of Xi'an Jiaotong University for structural and optical characterization. We also thank Engineer Xiaojing Zhang at School of Physics, Xi'an Jiaotong University for transmission electron microscopy instrument support.

Electronic Supplementary Material: Supplementary material (synthesis details and SEM images, CD spectra, and other characterization data of samples) is available in the online version of this article at https://doi.org/10.1007/s12274-024-6582-9.

References

[1] Lv, J. W.; Gao, X. Q.; Han, B.; Zhu, Y. F.; Hou, K.; Tang, Z. Y. Self-assembled inorganic chiral superstructures. *Nat. Rev. Chem.* **2022**, *6*, 125–145.

[2] Zhang, D. W.; Li, M.; Chen, C. F. Recent advances in circularly polarized electroluminescence based on organic light-emitting diodes. *Chem. Soc. Rev.* **2020**, *49*, 1331–1343.

[3] Zhao, X. L.; Zang, S. Q.; Chen, X. Y. Stereospecific interactions between chiral inorganic nanomaterials and biological systems. *Chem. Soc. Rev.* **2020**, *49*, 2481–2503.

[4] Wang, Y.; Xu, J.; Wang, Y. W.; Chen, H. Y. Emerging chirality in nanoscience. *Chem. Soc. Rev.* **2013**, *42*, 2930–2962.

[5] Esmaeili, M.; Akbari, E.; George, K.; Rezvan, G.; Taheri-Qazvini, N.; Sadati, M. Engineering nano/microscale chiral self-assembly in 3D printed constructs. *Nano-Micro Lett.* **2024**, *16*, 54.

[6] Kitzmann, W. R.; Freudenthal, J.; Reponen, A. P. M.; VanOrman, Z. A.; Feldmann, S. Fundamentals, advances, and artifacts in circularly polarized luminescence (CPL) spectroscopy. *Adv. Mater.* **2023**, *35*, 2302279.

[7] Gao, C.; Gu, Y. Y.; Zhao, Y.; Qu, L. T. Recent development of integrated systems of microsupercapacitors. *Energy Mater. Adv.* **2022**, *2022*, 9804891.

[8] Ha, M. J.; Kim, J. H.; You, M.; Li, Q.; Fan, C. H.; Nam, J. M. Multicomponent plasmonic nanoparticles: From heterostructured nanoparticles to colloidal composite nanostructures. *Chem. Rev.* **2019**, *119*, 12208–12278.

[9] Zhang, D.; Ding, C. P.; Zheng, X. Y.; Ye, J. Z.; Chen, Z. H.; Li, J. H.; Yan, Z. J.; Jiang, J. H.; Huang, Y. J. Ultrasensitive and accurate diagnosis of urothelial cancer by plasmonic AuNRs-enhanced

fluorescence of near-infrared Ag_2S quantum dots. *Rare Met.* **2022**, *41*, 3828–3838.
[10] Lermusiaux, L.; Nisar, A.; Funston, A. M. Flexible synthesis of high-purity plasmonic assemblies. *Nano Res.* **2021**, *14*, 635–645.
[11] Cao, Z. L.; Gao, H.; Qiu, M.; Jin, W.; Deng, S. Z.; Wong, K. Y.; Lei, D. Y. Chirality transfer from sub-nanometer biochemical molecules to sub-micrometer plasmonic metastructures: Physiochemical mechanisms, biosensing, and bioimaging opportunities. *Adv. Mater.* **2020**, *32*, 1907151.
[12] Hentschel, M.; Schäferling, M.; Duan, X. Y.; Giessen, H.; Liu, N. Chiral plasmonics. *Sci. Adv.* **2017**, *3*, e1602735.
[13] Pan, J. H.; Wang, X. Y.; Zhang, J. J.; Zhang, Q.; Wang, Q. B.; Zhou, C. Chirally assembled plasmonic metamolecules from intrinsically chiral nanoparticles. *Nano Res.* **2022**, *15*, 9447–9453.
[14] Zhu, D. Z.; Yan, J. F.; Liang, Z. W.; Xie, J. W.; Bai, H. L. Laser stripping of Ag shell from Au@Ag nanoparticles. *Rare Met.* **2021**, *40*, 3454–3459.
[15] Zhao, Y.; Xu, C. L. DNA-based plasmonic heterogeneous nanostructures: Building, optical responses, and bioapplications. *Adv. Mater.* **2020**, *32*, 1907880.
[16] Kong, X. T.; Besteiro, L. V.; Wang, Z. M.; Govorov, A. O. Plasmonic chirality and circular dichroism in bioassembled and nonbiological systems: Theoretical background and recent progress. *Adv. Mater.* **2018**, *32*, 1801790.
[17] Gao, Q.; Tan, L. L.; Wen, Z. H.; Fan, D. D.; Hui, J. F.; Wang, P. P. Chiral inorganic nanomaterials: Harnessing chirality-dependent interactions with living entities for biomedical applications. *Nano Res.* **2023**, *16*, 11107–11124.
[18] Hao, C. L.; Wang, G. Y.; Chen, C.; Xu, J.; Xu, C. L.; Kuang, H.; Xu, L. G. Circularly polarized light-enabled chiral nanomaterials: From fabrication to application. *Nano-Micro Lett.* **2023**, *15*, 39.
[19] Guo, Z. L.; Yu, G.; Zhang, Z. G.; Han, Y. D.; Guan, G. J.; Yang, W. S.; Han, M. Y. Intrinsic optical properties and emerging applications of gold nanostructures. *Adv. Mater.* **2023**, *35*, 2206700.
[20] Zheng, G. C.; He, J. J.; Kumar, V.; Wang, S. L.; Pastoriza-Santos, I.; Pérez-Juste, J.; Liz-Marzán, L. M.; Wong, K. Y. Discrete metal nanoparticles with plasmonic chirality. *Chem. Soc. Rev.* **2021**, *50*, 3738–3754.
[21] Abbas, S. U.; Li, J. J.; Liu, X.; Siddique, A.; Shi, Y. X.; Hou, M.; Yang, K.; Nosheen, F.; Cui, X. Y.; Zheng, G. C. et al. Chiral metal nanostructures: Synthesis, properties and applications. *Rare Met.* **2023**, *42*, 2489–2515.
[22] Zhou, S.; Li, J. H.; Lu, J.; Liu, H. H.; Kim, J. Y.; Kim, A.; Yao, L. H.; Liu, C.; Qian, C.; Hood, Z. D. et al. Chiral assemblies of pinwheel superlattices on substrates. *Nature* **2022**, *612*, 259–265.
[23] Xu, L. G.; Wang, X. X.; Wang, W. W.; Sun, M. Z.; Choi, W. J.; Kim, J. Y.; Hao, C. L.; Li, S.; Qu, A. H.; Lu, M. R. et al. Enantiomer-dependent immunological response to chiral nanoparticles. *Nature* **2022**, *601*, 366–373.
[24] Lee, H. E.; Ahn, H. Y.; Mun, J.; Lee, Y. Y.; Kim, M.; Cho, N. H.; Chang, K.; Kim, W. S.; Rho, J.; Nam, K. T. Amino-acid- and peptide-directed synthesis of chiral plasmonic gold nanoparticles. *Nature* **2018**, *556*, 360–365.
[25] Zheng, J. P.; Boukouvala, C.; Lewis, G. R.; Ma, Y. C.; Chen, Y.; Ringe, E.; Shao, L.; Huang, Z. F.; Wang, J. F. Halide-assisted differential growth of chiral nanoparticles with threefold rotational symmetry. *Nat. Commun.* **2023**, *14*, 3783.
[26] Scarabelli, L.; Coronado-Puchau, M.; Giner-Casares, J. J.; Langer, J.; Liz-Marzán, L. M. Monodisperse gold nanotriangles: Size control, large-scale self-assembly, and performance in surface-enhanced raman scattering. *ACS Nano* **2014**, *8*, 5833–5842.
[27] Ni, B.; Zhou, J.; Stolz, L.; Cölfen, H. A facile and rational method to tailor the symmetry of Au@Ag nanoparticles. *Adv. Mater.* **2023**, *35*, 2209810.
[28] Germain, V.; Li, J.; Ingert, D.; Wang, Z. L.; Pileni, M. P. Stacking faults in formation of silver nanodisks. *J. Phys. Chem. B* **2003**, *107*, 8717–8720.
[29] Choi, B. K.; Kim, J.; Luo, Z.; Kim, J.; Kim, J. H.; Hyeon, T.; Mehraeen, S.; Park, S.; Park, J. Shape transformation mechanism of gold nanoplates. *ACS Nano* **2023**, *17*, 2007–2018.
[30] Wang, H. D.; Liu, Y.; Yu, J. M.; Luo, Y. G.; Wang, L. L.; Yang, T.; Raktani, B.; Lee, H. Selectively regulating the chiral morphology of amino acid-assisted chiral gold nanoparticles with circularly polarized light. *ACS Appl. Mater. Interfaces* **2022**, *14*, 3559–3567.
[31] Hong, J. W.; Lee, S. U.; Lee, Y. W.; Han, S. W. Hexoctahedral Au nanocrystals with high-index facets and their optical and surface-enhanced raman scattering properties. *J. Am. Chem. Soc.* **2012**, *134*, 4565–4568.
[32] Lee, H. E.; Yang, K. D.; Yoon, S. M.; Ahn, H. Y.; Lee, Y. Y.; Chang, H.; Jeong, D. H.; Lee, Y. S.; Kim, M. Y.; Nam, K. T. Concave rhombic dodecahedral Au nanocatalyst with multiple high-index facets for CO_2 reduction. *ACS Nano* **2015**, *9*, 8384–8393.
[33] Lin, H. X.; Lei, Z. C.; Jiang, Z. Y.; Hou, C. P.; Liu, D. Y.; Xu, M. M.; Tian, Z. Q.; Xie, Z. X. Supersaturation-dependent surface structure evolution: From ionic, molecular to metallic micro/nanocrystals. *J. Am. Chem. Soc.* **2013**, *135*, 9311–9314.
[34] Nguyen, Q. N.; Wang, C. X.; Shang, Y. X.; Janssen, A.; Xia, Y. N. Colloidal synthesis of metal nanocrystals: From asymmetrical growth to symmetry breaking. *Chem. Rev.* **2023**, *123*, 3693–3760.
[35] Yang, F.; Feng, J.; Chen, J. X.; Ye, Z. Y.; Chen, J. H.; Hensley, D. K.; Yin, Y. D. Engineering surface strain for site-selective island growth of Au on anisotropic Au nanostructures. *Nano Res.* **2023**, *16*, 5873–5879.
[36] Cho, N. H.; Byun, G. H.; Lim, Y. C.; Im, S. W.; Kim, H.; Lee, H. E.; Ahn, H. Y.; Nam, K. T. Uniform chiral gap synthesis for high dissymmetry factor in single plasmonic gold nanoparticle. *ACS Nano* **2020**, *14*, 3595–3602.
[37] Ni, B.; Mychinko, M.; Gómez-Graña, S.; Morales-Vidal, J.; Obelleiro-Liz, M.; Heyvaert, W.; Vila-Liarte, D.; Zhuo, X. L.; Albrecht, W.; Zheng, G. C. et al. Chiral seeded growth of gold nanorods into fourfold twisted nanoparticles with plasmonic optical activity. *Adv. Mater.* **2023**, *35*, 2208299.
[38] Zheng, Y. L.; Wang, Q.; Sun, Y. W.; Huang, J.; Ji, J.; Wang, Z. J.; Wang, Y. W.; Chen, H. Y. Chiral active surface growth via glutathione control. *Adv. Opt. Mater.* **2023**, *11*, 2202858.
[39] Huang, J. F.; Zhu, Y. H.; Liu, C. X.; Shi, Z.; Fratalocchi, A.; Han, Y. Unravelling thiol's role in directing asymmetric growth of Au nanorod-Au nanoparticle dimers. *Nano Lett.* **2016**, *16*, 617–623.
[40] Yan, J.; Chen, Y. D.; Hou, S.; Chen, J. Q.; Meng, D. J.; Zhang, H.; Fan, H. Z.; Ji, Y. L.; Wu, X. C. Fabricating chiroptical starfruit-like Au nanoparticles via interface modulation of chiral thiols. *Nanoscale* **2017**, *9*, 11093–11102.
[41] Ben-Moshe, A.; Wolf, S. G.; Bar Sadan, M.; Houben, L.; Fan, Z. Y.; Govorov, A. O.; Markovich, G. Enantioselective control of lattice and shape chirality in inorganic nanostructures using chiral biomolecules. *Nat. Commun.* **2014**, *5*, 4302.
[42] Vishnevetskii, D. V.; Mekhtiev, A. R.; Perevozova, T. V.; Ivanova, A. I.; Averkin, D. V.; Khizhnyak, S. D.; Pakhomov, P. M. L-Cysteine as a reducing/capping/gel-forming agent for the preparation of silver nanoparticle composites with anticancer properties. *Soft Matter* **2022**, *18*, 3031–3040.
[43] Wu, F. X.; Li, F. H.; Tian, Y.; Lv, X. L.; Luan, X. X.; Xu, G. B.; Niu, W. X. Surface topographical engineering of chiral Au nanocrystals with chiral hot spots for plasmon-enhanced chiral discrimination. *Nano Lett.* **2023**, *23*, 8233–8240.
[44] Su, A.; Wang, Q.; Huang, L. P.; Zheng, Y. L.; Wang, Y. W.; Chen, H. Y. Gold nanohexagrams via active surface growth under sole CTAB control. *Nanoscale* **2023**, *15*, 14858–14865.
[45] Personick, M. L.; Mirkin, C. A. Making sense of the mayhem behind shape control in the synthesis of gold nanoparticles. *J. Am. Chem. Soc.* **2013**, *135*, 18238–18247.
[46] Shi, Y. F.; Lyu, Z. H.; Zhao, M.; Chen, R. H.; Nguyen, Q. N.; Xia, Y. N. Noble-metal nanocrystals with controlled shapes for catalytic and electrocatalytic applications. *Chem. Rev.* **2021**, *121*, 649–735.
[47] Meena, S. K.; Celiksoy, S.; Schäfer, P.; Henkel, A.; Sönnichsen, C.; Sulpizi, M. The role of halide ions in the anisotropic growth of gold nanoparticles: A microscopic, atomistic perspective. *Phys. Chem. Chem. Phys.* **2016**, *18*, 13246–13254.
[48] Yang, S. H.; Zheng, Y. L.; He, G. Y.; Zhang, M. M.; Li, H. Y.; Wang, Y. W.; Chen, H. Y. From flat to deep concave: An unusual mode of facet control. *Chem. Commun.* **2022**, *58*, 6128–6131.
[49] Zheng, Y. L.; Zong, J. P.; Xiang, T.; Ren, Q.; Su, D. M.; Feng, Y. H.; Wang, Y. W.; Chen, H. Y. Turning weak into strong: On the CTAB-induced active surface growth. *Sci. China Chem.* **2022**, *65*, 1299–1305.